Chapter VI: Microstructure, Cation distribution and Magnetic Properties of $Zn_xCo_{1-x}Cr_2O_4$ (x=0.05, 0.1) Nanoparticles.

6.1. Introduction

Rich sequence of magnetic transitions such as Curie transition (T_C), spin-spiral transition (T_S) and lock-in transition (T_L) have been reported in few chromites [Tomiyasu et al. (2004)]. In this context, Kemei *et al.* have studied magnetic transitions in normal spinel, $Mg_{1-x}Cu_xCr_2O_4$. They have reported that the Neel temperature (T_N) has been observed at 12.5 K at x=0 increases to 128 K at x=1 [Kemei et al. (2012)]. Durgesh *et al.* have observed an enhancement in T_C upto 200 K and spiral ordering temperature upto 40 K by increasing Fe concentration upto 50% [Durgesh et al. (2017)]. Kemei *et al.* have reported the changes in structural ground states of $ZnCr_2O_4$ when 10% and 20% Co^{2+} cations are substituted on the nonmagnetic, Zn^{2+} site. It has been shown that when Co^{2+} ions are greater than or equal to 10%, the structural distortions that accompany antiferromagnetic ordering in $ZnCr_2O_4$ is suppressed [Kemei et al. (2014)]. The exciting results thus demands to be discussed after mixing A or B sites by magnetic or non-magnetic ions when size of the particles are reduced to nanometer range. The sequence of magnetic transitions such as T_C, T_S and T_L reported in few chromites, particularly $CoCr_2O_4$ have not been studied by substituting Zn so far. Hence, we examine the structural and microstructural evolution in $Zn_xCo_{1-x}Cr_2O_4$ (x=0.05, 0.1) nanoparticles and its magnetic ordering temperatures in the present chapter after synthesizing them in nanometer range. Structure and microstructures are investigated in these nanoparticles using XRD, XPS, TEM and EXAFS experiments. The magnetic transitions are examined through temperature dependent magnetization and neutron scattering using polarized neutron. The interparticle interaction is studied through temperature dependent ac susceptibility measurement done at 3, 31, 299 and 966 Hz.

We have discussed the cation distribution, structure and microstructure of $Zn_xCo_{1-x}Cr_2O_4$ (x=0.05, 0.1) nanoparticles in section 6.2.1. Section 6.2.2 discusses the magnetic properties and we have summarized the results in section 6.3.

6.2. Results

6.2.1. Structural and Microstructural analysis

6.2.1.1. X-ray Photoelectron Spectroscopy

X-ray Photoelectron Spectroscopy (XPS) technique is used to investigate the valency of transition metals in $Zn_xCo_{1-x}Cr_2O_4$ (x=0.05, 0.1). Figure 6.2.1 (a) and 6.2.1 (b) shows the characteristic core-level spectra of Co 2p and Cr 2p of $Zn_xCo_{1-x}Cr_2O_4$ (x=0.05, 0.1) fitted with two Gaussian peaks using XPS peak 4.1 software with Shirley background. The two strong peaks observed at 782.8 eV and 798.3 eV, shown in Fig. 6.2.1 (a) correspond to Co $2p_{3/2}$ and Co $2p_{1/2}$ respectively. The binding energy difference between $2p_{1/2}$ and $2p_{3/2}$ sublevels of Co 2p are found to be 15.5 eV and 15.4 eV for x=0.05 and 0.1 respectively. The observed difference in binding energy between two sublevels of Co, confirms +2 oxidation state of Co [Okamoto et al. (1975)].

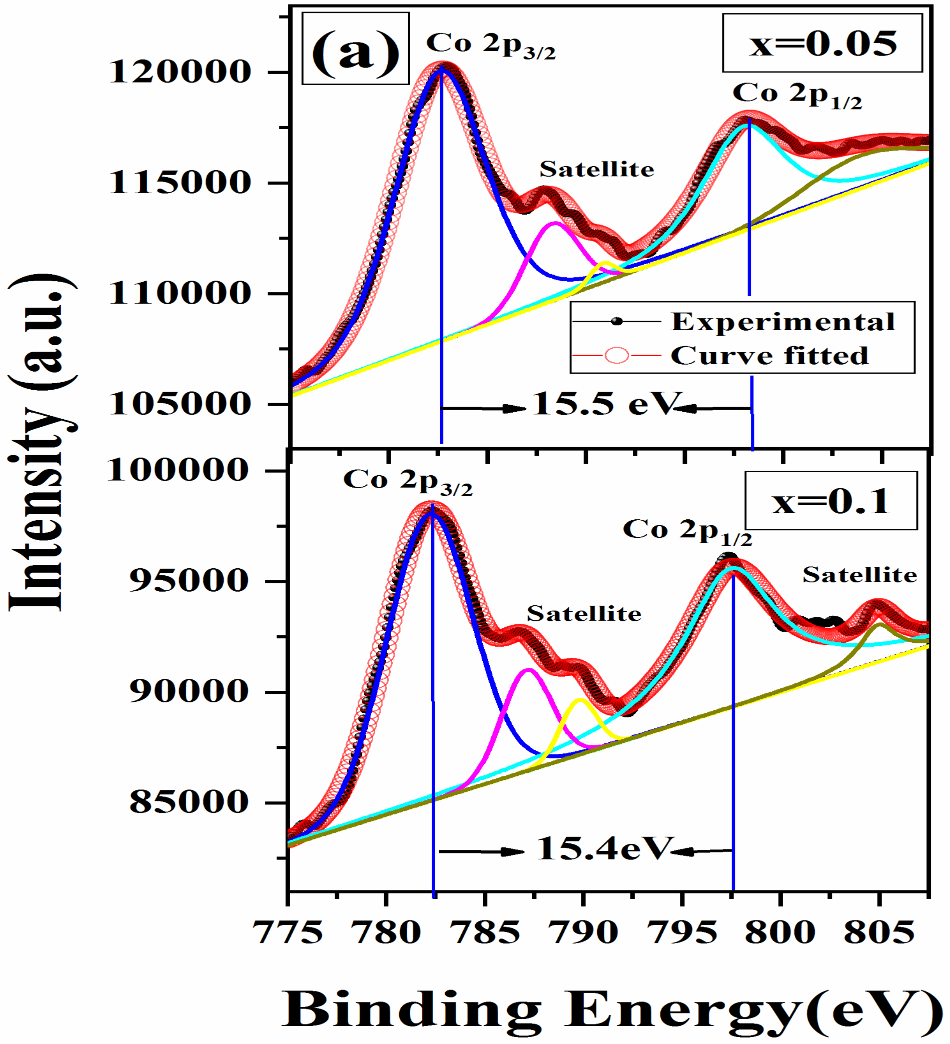
(a)
x=0.05
Co 2p3/2
Co 2p1/2
Satellite
Experimental
Curve fitted
15.5 eV
x=0.1
Co 2p3/2
Co 2p1/2
Satellite
Satellite
15.4eV
Intensity (a.u.)
120000
115000
110000
105000
100000
95000
90000
85000
775
780
785
790
795
800
805
Binding Energy(eV)

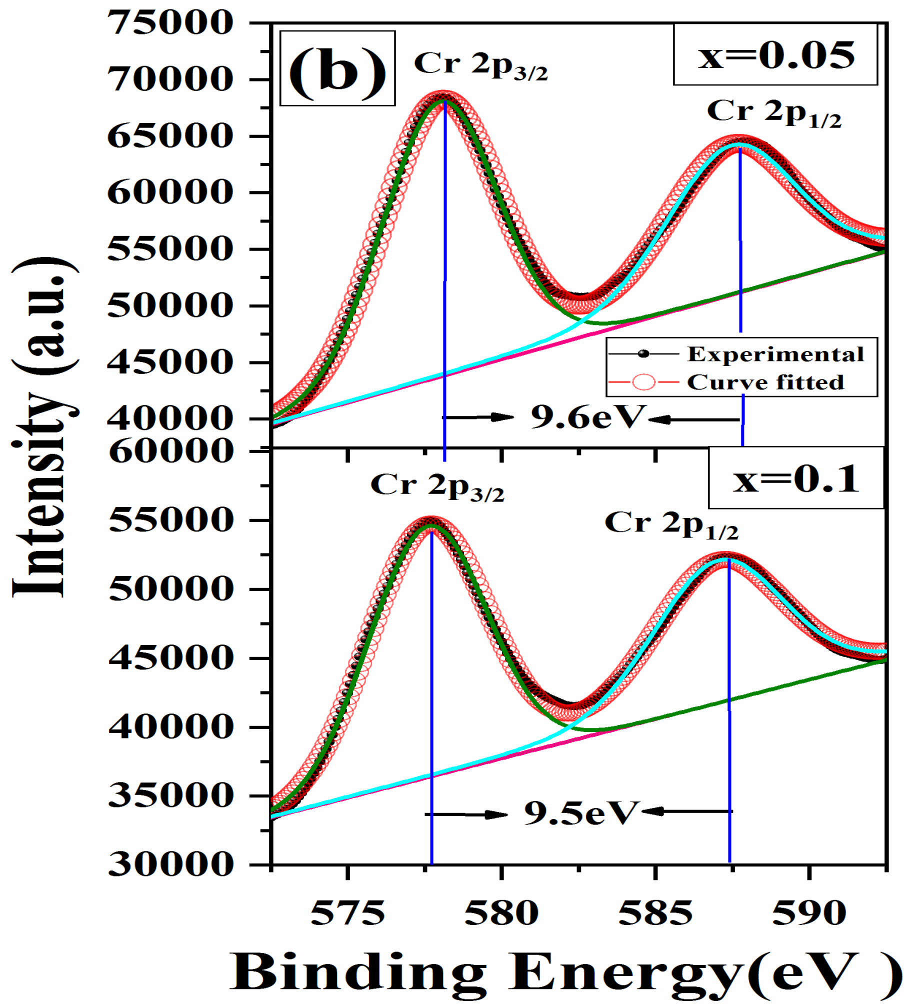

Figure 6.2.1 (a) and (b) X-ray photoelectron spectroscopy of Co and Cr for $Zn_xCo_{1-x}Cr_2O_4$, x= 0.05 and 0.1.

The satellite peaks observed at higher binding energy compared to their core peak could be due to shake up process of the Co 2p level. The obtained binding energy difference between $2p_{1/2}$ and $2p_{3/2}$ sublevels of chromium, shown in Fig. 6.2.1.(b) are 9.6 eV and 9.5

eV for x=0.05 and 0.1 respectively which confirms the +3 oxidation state of chromium [Okamoto et al. (1975)].

6.2.1.2. X-ray Diffraction

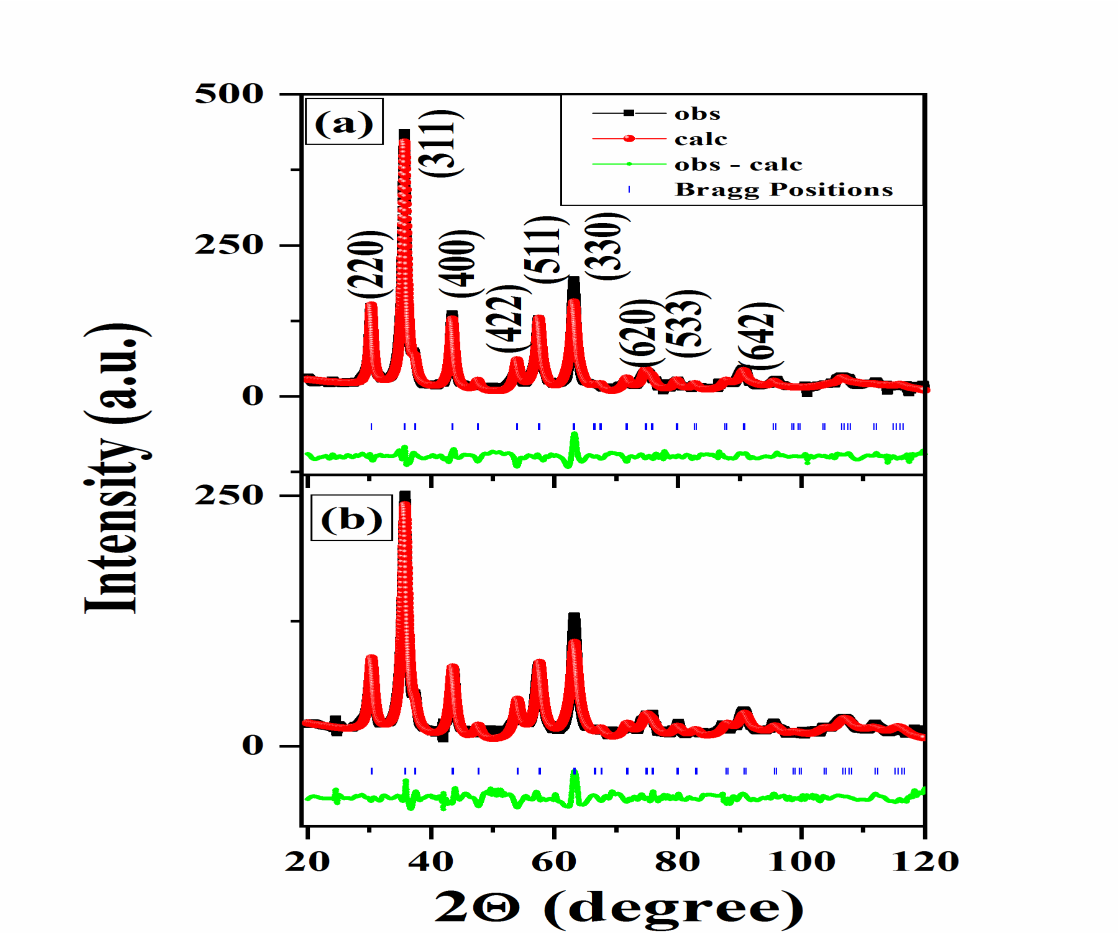

Fig. 6.2.1.2 X-ray diffraction (XRD) patterns of $Zn_xCo_{1-x}Cr_2O_4$ for **(a)** x=0.05 and **(b)** x=0.1, fitted with the space group $Fd\bar{3}m$ using the Le-Bail profile refinement.

Fig. 6.2.1.2 depicts the X-ray diffraction patterns of $Zn_xCo_{1-x}Cr_2O_4$ (x=0.05, 0.1). The prominent Bragg peaks at 30.45, 35.75, 43.5, 54, 57.5 and 63.1 degrees correspond to (220), (311), (400), (422), (511) and (440) of the cubic phase of $CoCr_2O_4$ (JCPCS file no: 780711) respectively. No characteristic reflection peaks derived from other contaminants such as $CoCr_2O_4$, cobalt or chromium oxides are detected, which eliminate the presence of impurities within the detection limit of the XRD instrument. All XRD patterns are fitted well with $Fd\bar{3}m$ space group using the Le-bail profile fitting of Fullprof program. In 6.2.1.2, solid line with square represents observed pattern, sphere represents calculated data after fitting and the difference between observe and calculated data is shown in bottom line. The Bragg peaks are represented by the tick marks above the difference plot. The lattice parameter (a) obtained from Le-Bail profile refinement decreases from 8.32 Å to 8.31 Å with increase in Zn concentration from 5 to 10 mol%. Although the ionic radius of Zn^{2+} is 0.74 Å, which is slightly higher than that of Co^{2+} ion (0.72 Å), we have observed a small contraction instead of expansion in unit cell volume with increase in Zn concentration. Similar decrease in unit cell volume is also observed by Melot *et al*. in bulk $Co_xZn_{1-x}Cr_2O_4$ [Melot et al. (2009)]. The possible reason behind the contraction of unit cell volume could be due to less ionic nature of Zn than Co, and/or due to decrease in A-B repulsion. The crystallite size of $Zn_xCo_{1-x}Cr_2O_4$ (x=0.05, 0.1) samples are estimated using Debye-Scherrer formula shown in equation (1), after correcting the instrumental broadening.

$$\mathbf{D_{XRD}} = \frac{0.89\,\lambda}{\beta\cos\Theta} \text{ ---------------------------(1)}$$

D_{XRD} is crystallite the size, λ is the wavelength of X-ray, β is the full width at half-maximum (FWHM), Θ is the Bragg angle. The mean crystallite size is found to be ~10 nm for both x= 0.05 and 0.1 samples.

6.2.1.3. Transmission Electron Microscope

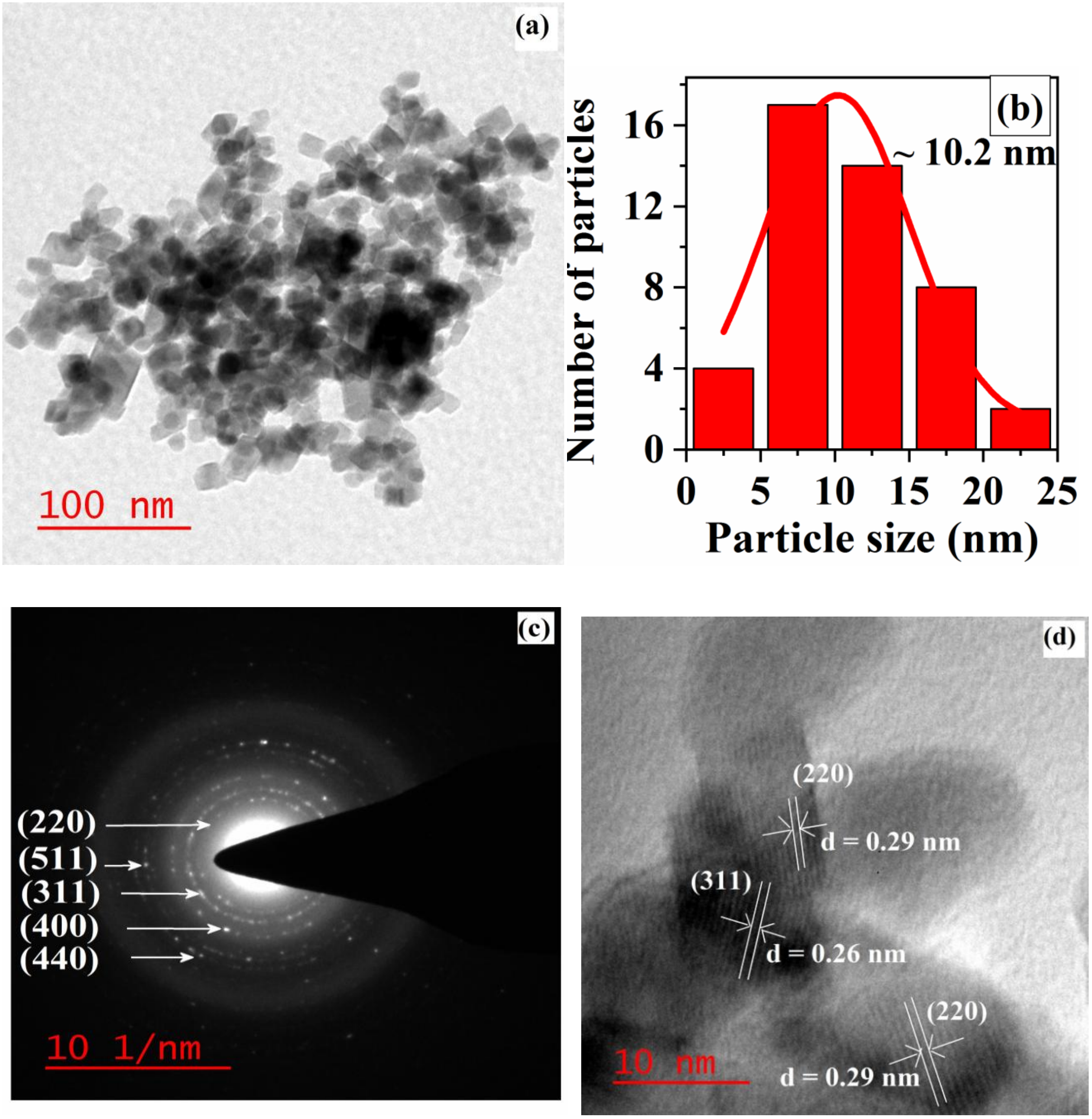

Fig. 6.2.1.3 Transmission electron micrographs of $Zn_{0.05}Co_{0.95}Cr_2O_4$ **(b)** Particle size histogram **(c)** Selective Area Electron Diffraction (SAED) pattern and **(d)** High resolution TEM image.

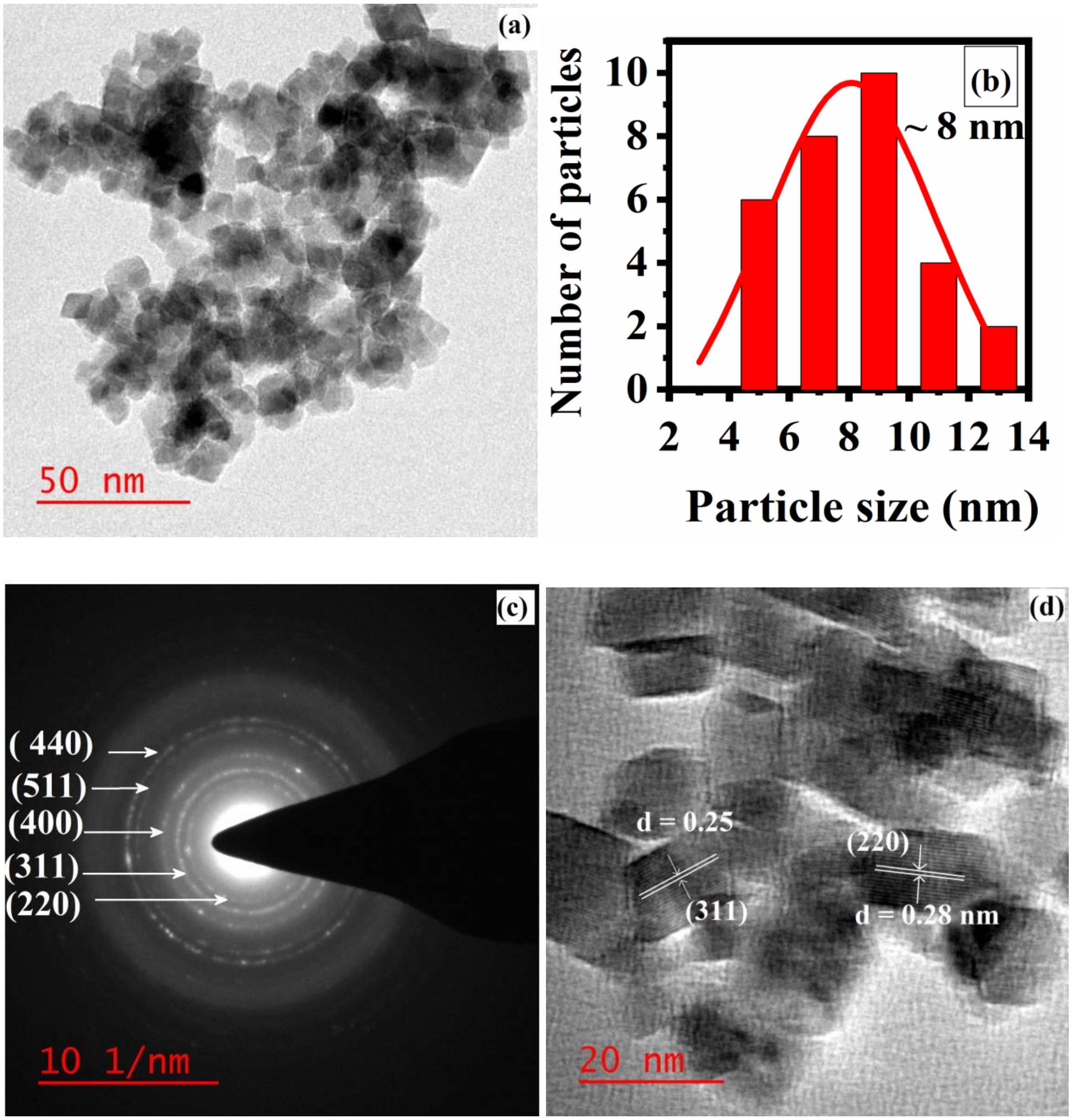

Fig. 6.2.1.4 (a) Transmission electron micrograph of $Zn_{0.1}Co_{0.9}Cr_2O_4$ **(b)** Particle size histogram **(c)** Selective Area Electron Diffraction (SAED) pattern and **(d)** High resolution TEM image.

Fig. 6.2.1.3 (a) and 6.2.1.4 (a) depict the transmission electron micrographs for x=0.05 and 0.1 respectively. The micrographs show well distributed particles of cuboid shape. From the particle size histogram shown in Fig. 6.2.1.3 (b) and 6.2.1.4 (b), the average particle size is found to be ~10 and ~8 nm for x=0.05 and 0.1 respectively, which match well with the crystallite size estimated from Scherrer's equation. The distinguished diffraction rings observed from the selected area electron diffraction (SAED) pattern, depicted in Fig. 6.2.1.3 (c) and 6.2.1.4 (c), indexed as (220), (311), (400), (440) and (511) of Fd-3m. Fig. 6.2.1.3 (d) and 6.2.1.4 (d) depict the high resolution TEM images of well defined atomic planes. The interplanar spacing of ~0.29 nm and ~0.26 nm corresponds to (220) and (311) of Fd-3m, cubic structure in both samples.

6.2.1.4. Extended X-ray Absorption Fine Structure

Although crystallite size does not change with Zn concentration, we have studied the cation distribution using EXAFS in x=0.05 and 0.1 as Zn strongly prefers the A-site. EXAFS analysis for Co, Zn and Cr K-edges have been carried out using Athena and Artemis program coupled with the FEFF 8.0 code for $Zn_xCo_{1-x}Cr_2O_4$ (x=0.05, 0.1).

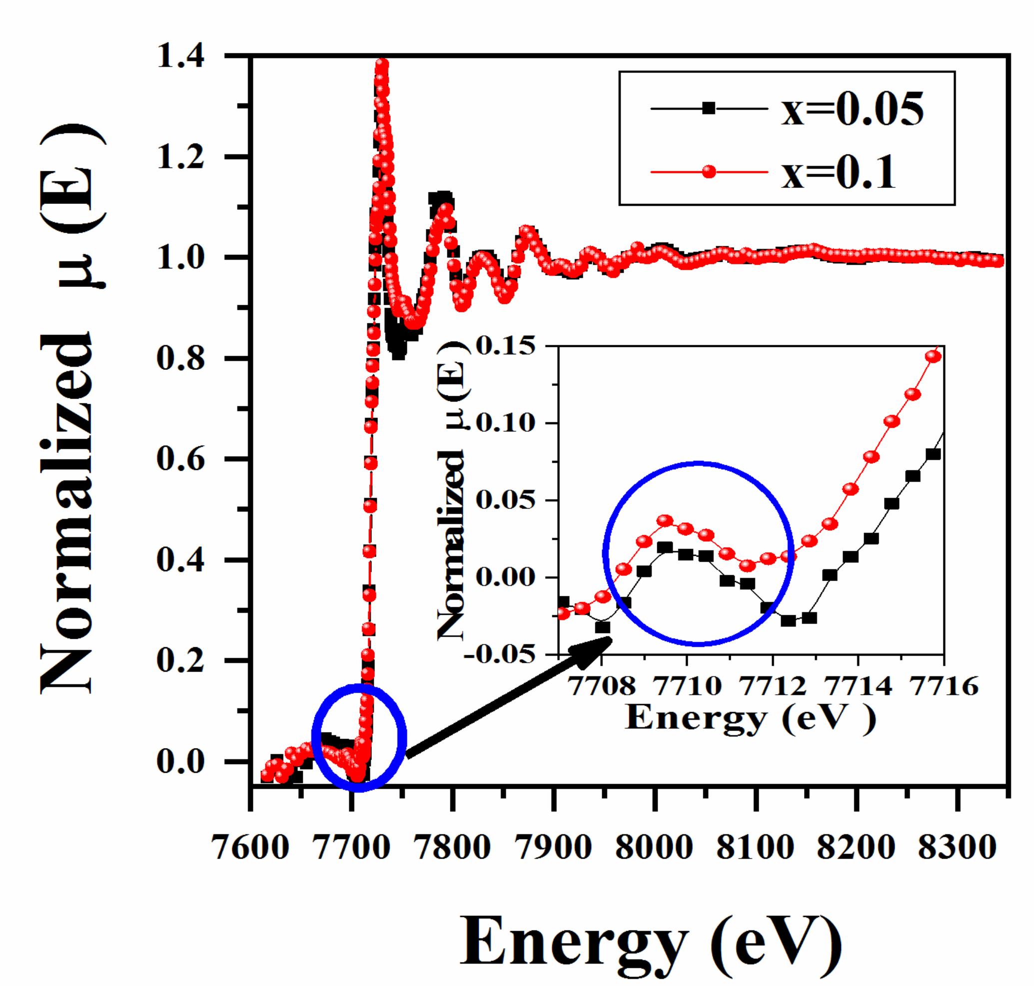

Fig. 6.2.1.5 Comparison of the EXAFS spectra of Co K-edge for $Zn_xCo_{1-x}Cr_2O_4$ (x=0.05, 0.1) nanoparticles. The inset show the expanded view of the pre-edge peak.

Fig. 6.2.1.5 depicts the normalized absorption versus energy for Co K-edge. Comparing the maximum absorption peak (K-edge) in EXAFS spectra of Co, Cr and Zn with standard samples of CoO, YCr_2O_3 and ZnO it is confirmed that valence of Zn, Co and Cr are in +2, +2 and +3 respectively. In addition, we observed that the energy of K-edge peak does not change with increase in Zn concentration. While the main peak in Co spectra is associated with a small pre-edge peak (Inset of Fig. 6.2.1.5), the same is absent in both Cr and Zn K-edges. While the main peak observed in Co spectra is attributed to

1s to 4p transition, the pre-edge peak is due to 1s to 3d quadrapole and from 1s to 3d/4p (hybridized orbitals) dipole transitions [Groot et al. (2001); Grunes et al. (1983)]. The intensity of quadrupole transition is in general very low and the degree of hybridization of the transition metal 3d states with 4p states affects the pre-edge peak intensity which in turn is affected by the degree of centrosymmetry of the photon absorber. The mixing of the 4p and 3d orbitals is forbidden in octahedral site due to the presence of inversion symmetry and it is allowed in the tetrahedral symmetry [Groot et al. (2001); Grunes et al. (1983)]. Absence of pre-edge peak in Cr K-edge confirms that Cr occupies the B site. However absence of pre-edge peak in Zn is due to completely filled 3d states of Zn [Aquilanti et al. (2011)]. The pre-edge peak intensity of Co increases with increase in Zn concentration which indicates that Co prefers tetrahedral symmetry. Further, the qualitative information about the local structure around Zn, Co and Cr atoms could be obtained from the Fourier transform of the respective K-edge spectra.

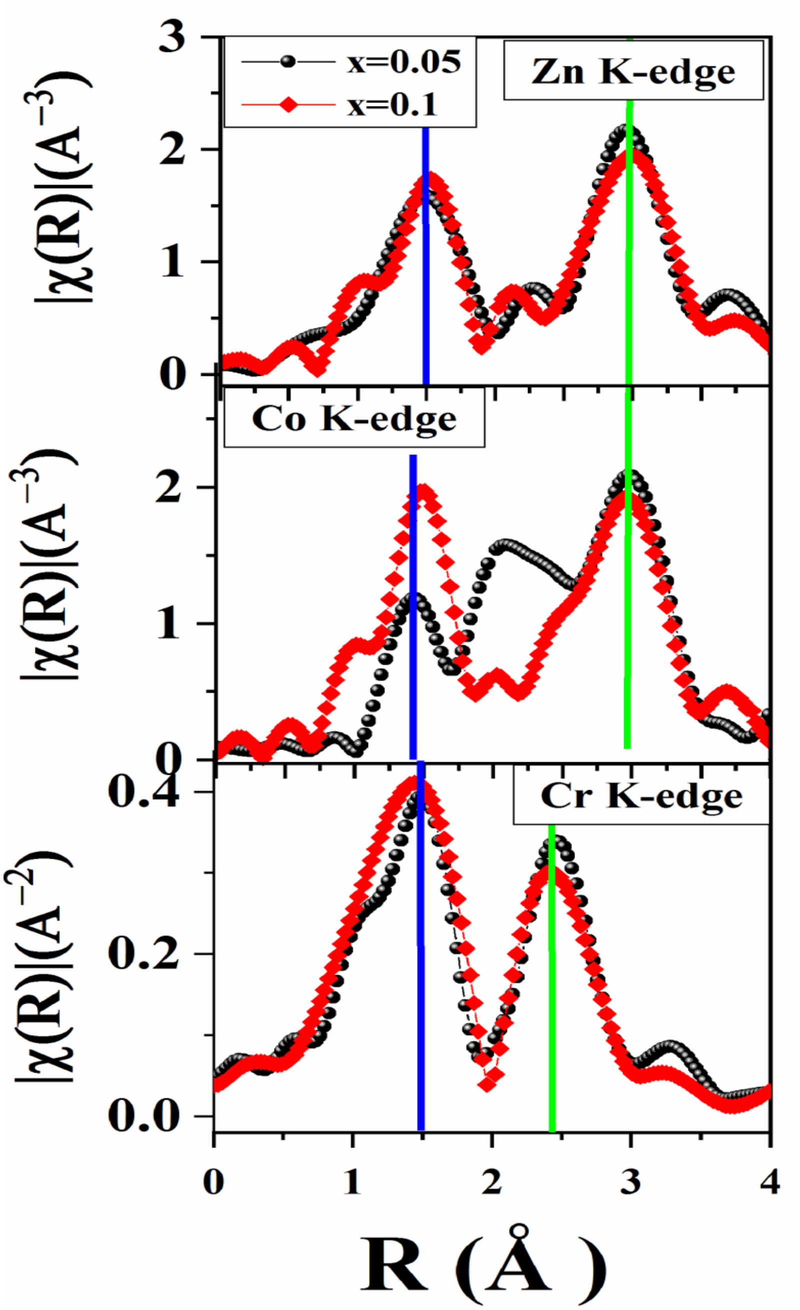

Fig. 6.2.1.6 Fourier transforms moduli of the χ(R) EXAFS signals for Zn, Co and Cr K-edges data.

Fig. 6.2.1.6 depicts the Fourier transform in R-space for Zn, Co and Cr respectively. In ferrites, the radial distance of the first coordinate shell is considered to differentiate the site distribution of cations at the A and B sites. $CoCr_2O_4$ crystallizes in normal spinel structure with Co preferring A site and Cr occupying B site. The radial distribution of the first coordination shell in Co and Cr environments is found to be 1.6 Å in $CoCr_2O_4$ [Jagadish et al. (2016)]. The position of second peak (i.e. the distance of second coordination shell) observed at different radial distances, is considered to determine the distribution of cations in two different environments. Similarly in present case, we also observe the first coordination shell to be nearly same (~1.6 Å) in Zn, Co and Cr which eliminates the possibility of finding the distribution of the cations in A and B sites. Therefore, the position of the second coordination shell is taken into consideration to determine the distribution of cations. In the case of Zn and Co, the position of second peak is observed at r ~ 3 Å which indicates that Zn and Co prefer to occupy the A site. In case of Cr, the position of second peak is observed at r ~ 2.45 Å which indicates that Cr prefers to occupy the B site. After obtaining the qualitative idea of the local structure around Zn, Co and Cr, we have fitted the reduced EXAFS data in R-space. The raw FT-EXAFS spectra, background corrected and energy calibrated spectra are fitted using IFEFFIT (ARTEMIS) software for Zn, Co and Cr in x=0.05 and 0.1 in order to obtain the bond distance (r) and mean-square disorder parameter (σ^2). It is well known that σ^2, the amplitude function, which is the mean-square displacement of the path-length due to the thermal or static disorder and is strongly correlated with the number of nearest neighbors. Lattice parameters and atomic coordinates are used as inputs to generate a FEFF input file, with Cr, Zn and/or Co as the core for the corresponding Cr, Zn and/or Co K-edge spectra. As Zn replaces Co at A-site, we have used the atomic coordinates of Co to fit the Zn K-edge.

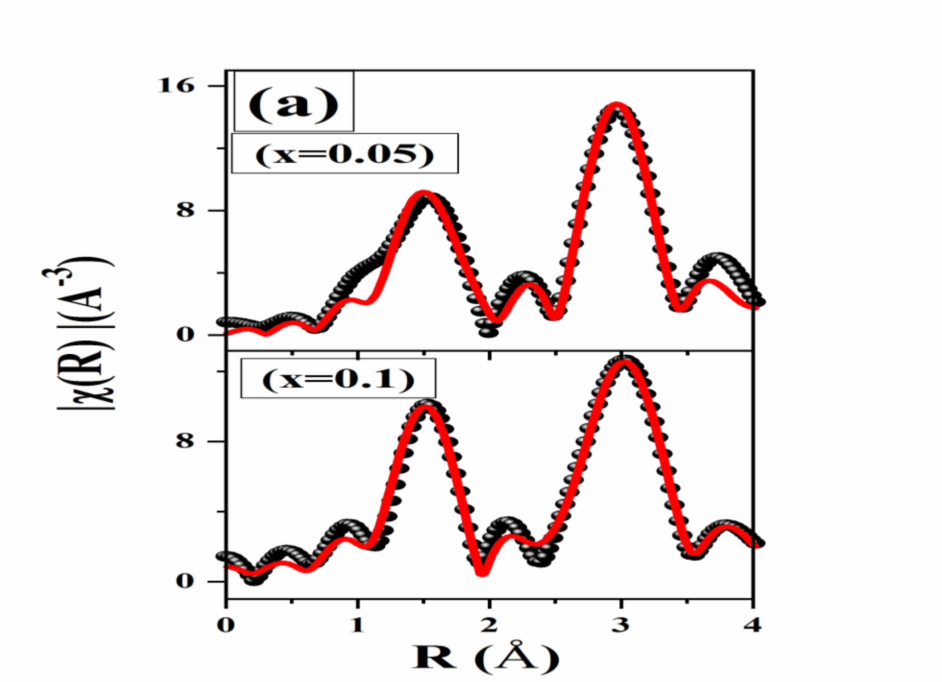
(a)
(x=0.05)
(x=0.1)
|χ(R)|(A^-3)
16
8
0
8
0
0
1
2
3
4
R (Å)

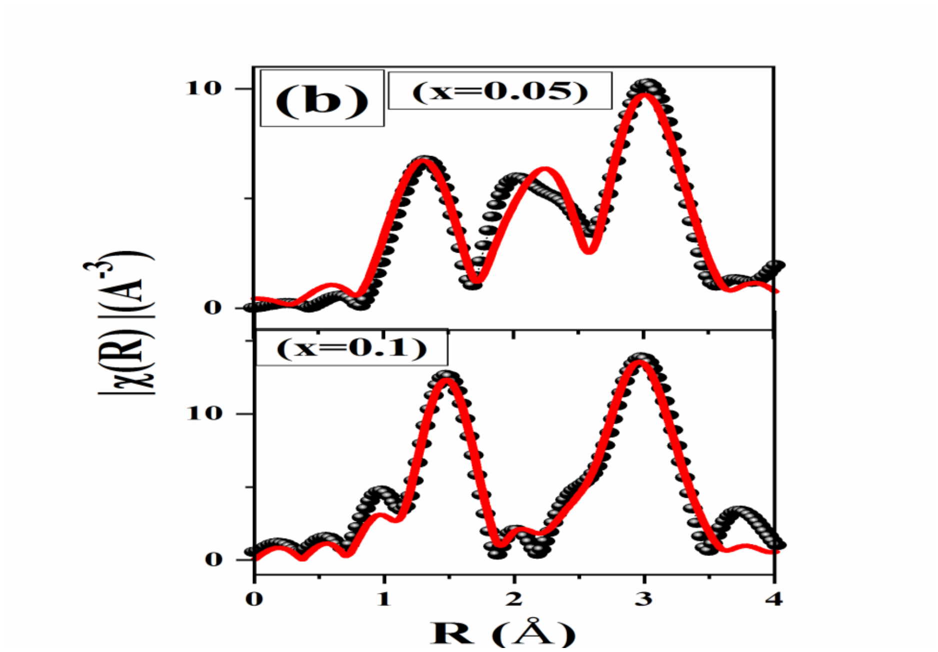
(b)
(x=0.05)
(x=0.1)
|χ(R)|(A^-3)
10
0
10
0
0
1
2
3
4
R (Å)

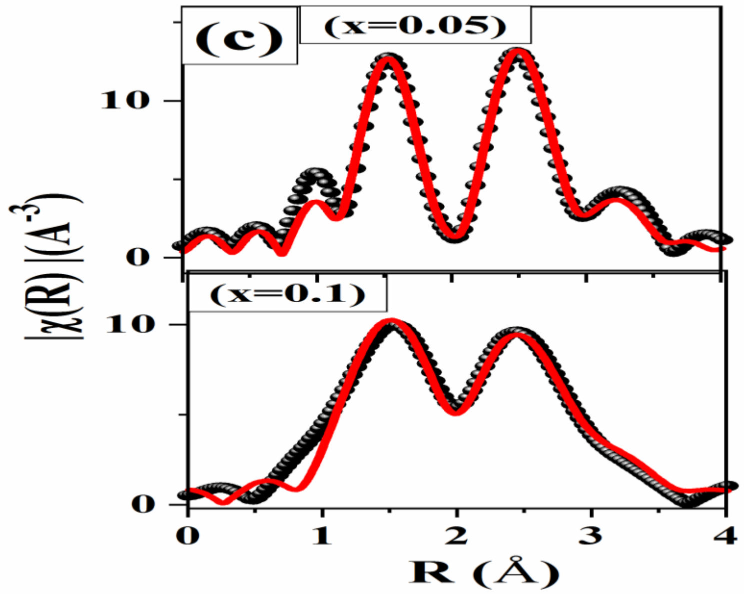

Fig. 6.2.1.7 (a) Zn K- edge, **(b)** Co K-edge and **(c)** Cr K-edge Fourier transform EXAFS data with real (r) parts of the phase plotted with fitted curves for $Zn_xCo_{1-x}Cr_2\,O_4$ (x=0.05, 0.1).

Table 6.2.1: Fitting parameters like bond length, disorder factors deduced from EXAFS fitting (a) Zn K-edge (b) Co K-edge and (c) Cr K-edge respectively.

(a) Zn edge			
Path	**Parameter**	**x= 0.05**	**x= 0.1**
Zn-O	**$r/^{o}A$**	1.95	1.94
	σ^2	0.009	0.002
Zn-Cr	**$r/^{o}A$**	3.46	3.46
	σ^2	0.0013	0.0055
Zn-O	**$r/^{o}A$**	3.41	3.2
	σ^2	0.0017	0.0064
Zn-Zn	**$r/^{o}A$**	3.626	3.62
	σ^2	0.0023	0.0045
(b) **Co edge**			
Path	**Parameter**	**x= 0.05**	**x= 0.1**
Co-Cr	**$r/^{o}A$**	1.96	1.94
	σ^2	0.0026	0.0031
Co-Cr	**$r/^{o}A$**	3.48	3.42
	σ^2	0.0039	0.0089
Co-O	**$r/^{o}A$**	3.40	3.27
	σ^2	0.0083	0.0437
Co-Co	**$r/^{o}A$**	2.63	2.19
	σ^2	0.0068	0.0235
(C) Cr edge			
Path	**Parameter**	**x=0.05**	**x=0.1**
Co-O	**$r/^{o}A$**	1.964	1.965
	σ^2	0.0026	0.0019
Cr-Cr	**$r/^{o}A$**	2.91	2.96
	σ^2	0.0039	0.0028
Cr-Co	**$r/^{o}A$**	3.407	3.339
	σ^2	0.0083	0.0147

The photoelectron scattering paths are then calculated and the experimental data are fitted up to 4 Å in the R-space and the results are as shown in Fig. 6.2.1.7**.** From Table 6.2.1, we notice that the bond length (r) observed between the central atom and second coordination shell of Co, Zn and Cr are 3.48 Å, 3.46 Å and 2.91 Å for x =0.05. It is observed that there is no significant change in bond length with increase in Zn concentration. Hence we conclude that Co and Zn ions occupy the A site and Cr strongly prefers the B site. The results corroborates with our previous report on $CoCr_2O_4$ where we have shown that Co atoms are tetrahedrally coordinated by 12 Cr ions at 3.45 Å as second nearest neighbors and Cr atoms are octahedrally coordinated by 6 Cr ions at 2.96 Å as the second nearest neighbours.

6.2.2. Magnetic Properties

6.2.2.1. Temperature dependent magnetization

While the cation distribution does not change by incorporating Zn in $CoCr_2O_4$, we further examine the effect on magnetic properties by analyzing the temperature and external magnetic field dependent magnetization in $Zn_xCo_{1-x}Cr_2O_4$ (x=0.05, 0.1).

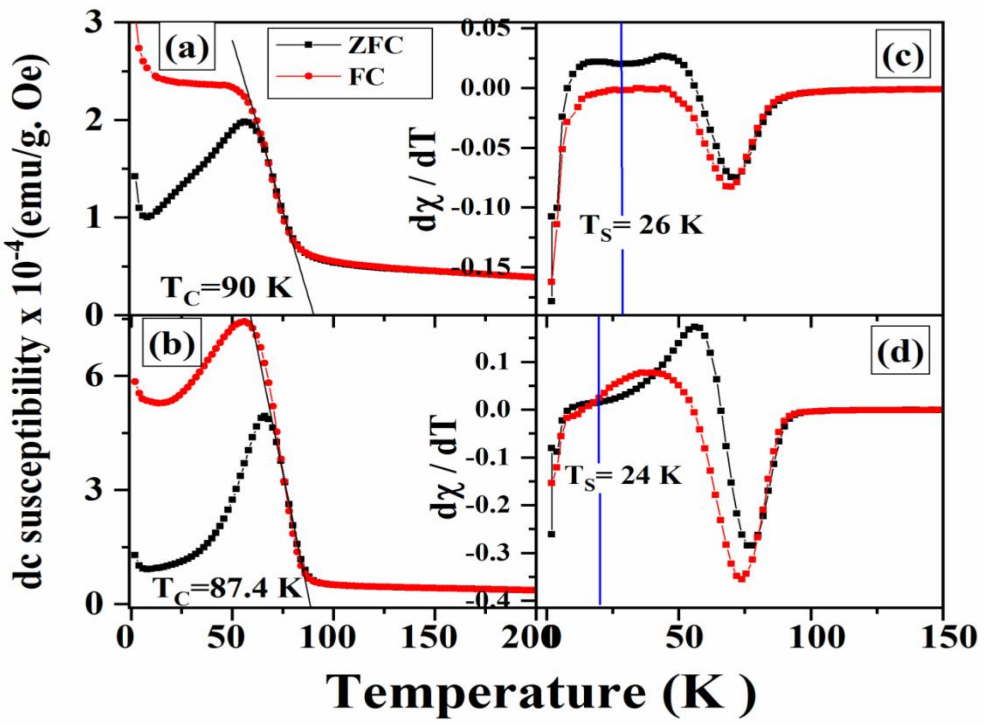

Fig. 6.2.2.1 Dc susceptibility vs. temperature at 500 Oe for $Zn_xCo_{1-x}Cr_2O_4$ **(a)** x=0.05 and **(b)** x=0.1. **(c)** and **(d)** show dχ/dT of x=0.05 and 0.1 respectively.

Fig. 6.2.2.1 depicts the temperature dependence of zero-field-cooled (ZFC) and field-cooled (FC) dc susceptibility with an applied field of 500 Oe. With decrease in temperature from 300 K, around 80 K, both M_{FC} and M_{ZFC} show a rapid increase, which is indicative of paramagnetic to long-range ferrimagnetic transition, i.e., T_C. It is derived by extrapolating the linear part of magnetization to zero in the high temperature regime. T_C is found to be 90 K and 87.4 K for x=0.05 and 0.1 respectively which is lower than that of T_C of bulk and polycrystalline $CoCr_2O_4$ (95 K and 97 K) [Yamasaki et al. (2006); Plumier et al. (1968); Lawes et al. (2006)]. As T_C is decided by A-B exchange interaction in spinels, decrease in T_C with increase in Zn concentration thus confirms that A-B exchange interaction decreases due to replacement of Co^{2+} by non-magnetic, Zn^{2+} at A site. With decrease in temperature, both M_{ZFC} and M_{FC} show a large increase and reaches to a maximum at temperature T_{max}, followed by a splitting at a temperature called irreversible temperature, T_{irr}. T_{max} and T_{irr} observed at 56 K and 66 K respectively in x=0.05, which shift to 66 K and 73 K respectively with increase in Zn concentration to 10 mol%. Higher values of T_{irr} than T_{max} in both samples indicate the presence of large spin clusters which are ordered at higher temperature. T_{max} generally indicates either the blocking temperature (T_B) of superparamagnets or the spin-freezing temperature (T_f) of spin glasses, which could be further confirmed from ac susceptibility measurement. $d\chi/dT$ depicted in Fig. 6.2.2.1 (c) and (d) show, in addition to T_C at 90 K and 87.4 K, an anomaly at 26 K and 24 K which is the spiral-spiral transition, T_S for x=0.05 and 0.1 respectively. In bulk and single crystals of $CoCr_2O_4$ while T_S is observed at 31 K and 24 K in case of nanoparticles of $CoCr_2O_4$, we have shown T_S at ~ 25±1 K which remains unaffected by varying the size from 10 to 50 nm [Lawes et al. (2006); Tomiyasu et al.

(2004); Jagadish et al. (2016)]. Another magnetic anomaly corresponds to spin lock-in transition (T_L) observed at 15 K in single crystal of $CoCr_2O_4$ is found to be absent after incorporating Zn^{2+} in the present case [Tomiyasu et al. (2004)]. However we have shown in our previous work on $CoCr_2O_4$ that T_L increases from 5 K to 8.5 K with increase in size from 10 to 50 nm [Jagadish et al. (2016)].

6.2.2.2. Diffused Neutron Scattering using polarized neutrons

The spin-spiral transition (T_S) and spin lock-in transition (T_L) temperatures are further probed through Diffused Neutron Scattering (DNS) using polarized neutron source available at FRM II, Germany. Along three orthogonal directions, the sequence of magnetic transitions such as T_C, T_S and T_L are observed in $CoCr_2O_4$ are analyzed in the present work. The typical magnetic, nuclear and spin-incoherent scattering in $Zn_xCo_{1-x}Cr_2O_4$ (x=0.05, 0.1) particles is depicted in Fig. 6.2.2.2 (a) and (b) respectively. Magnetic Bragg peaks such as (111) and (220) have been measured in detail by spin flip scattering in the range of 3.5 K to 100 K. With decrease in temperature from 100 K, reflection of (111) peak is getting broad and asymmetric in both x= 0.05 and 0.1 as shown in Fig. 6.2.2.3. The fundamental reflections are coherent Bragg reflections up to 100 K and above that the intensity of the (111) reflection diminishes to the background level.

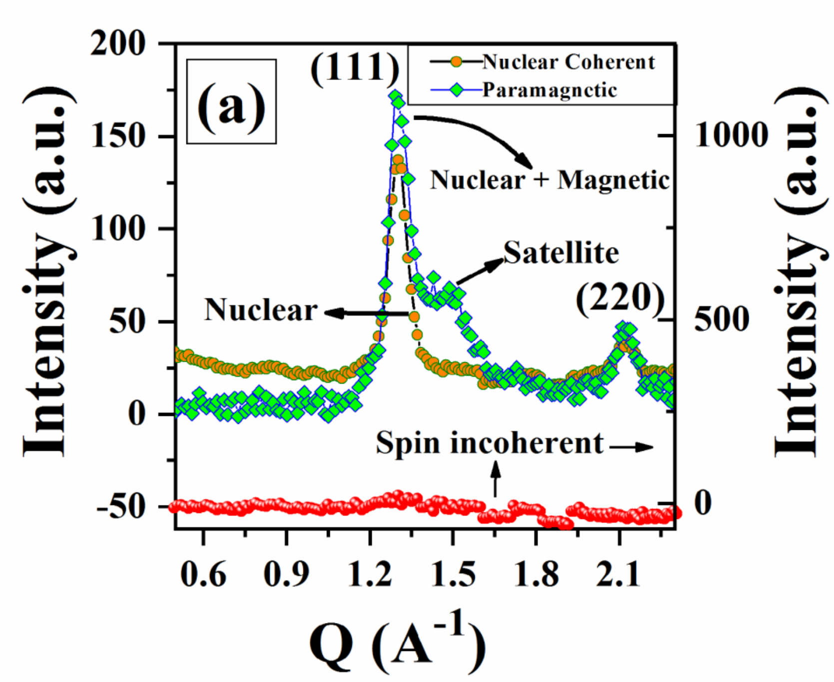

Fig. 6.2.2.2 (a) Polarized neutron scattering data showing nuclear, magnetic and spin-incoherent scattering for x=0.05.

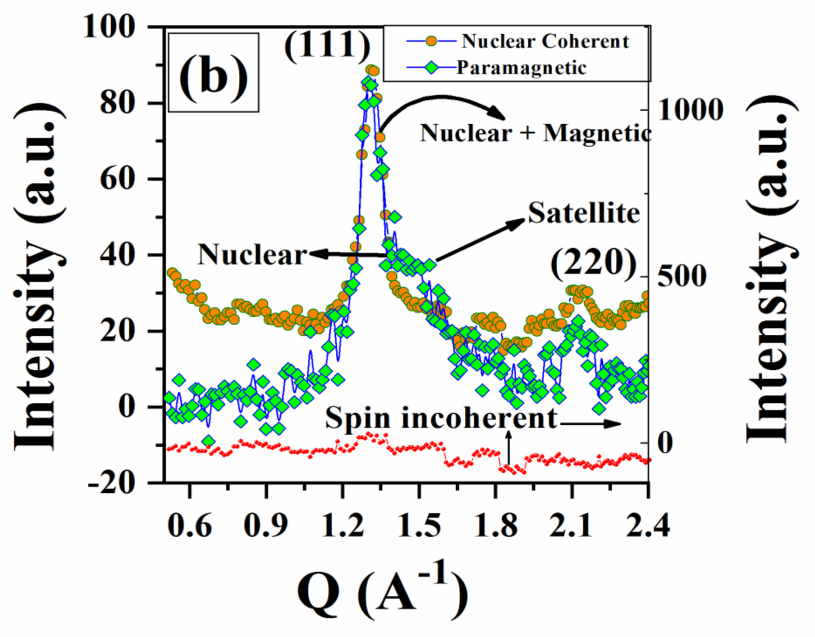

Fig. 6.2.2.2 (b) Polarized neutron scattering data showing nuclear, magnetic and spin-incoherent scattering for x=0.1.

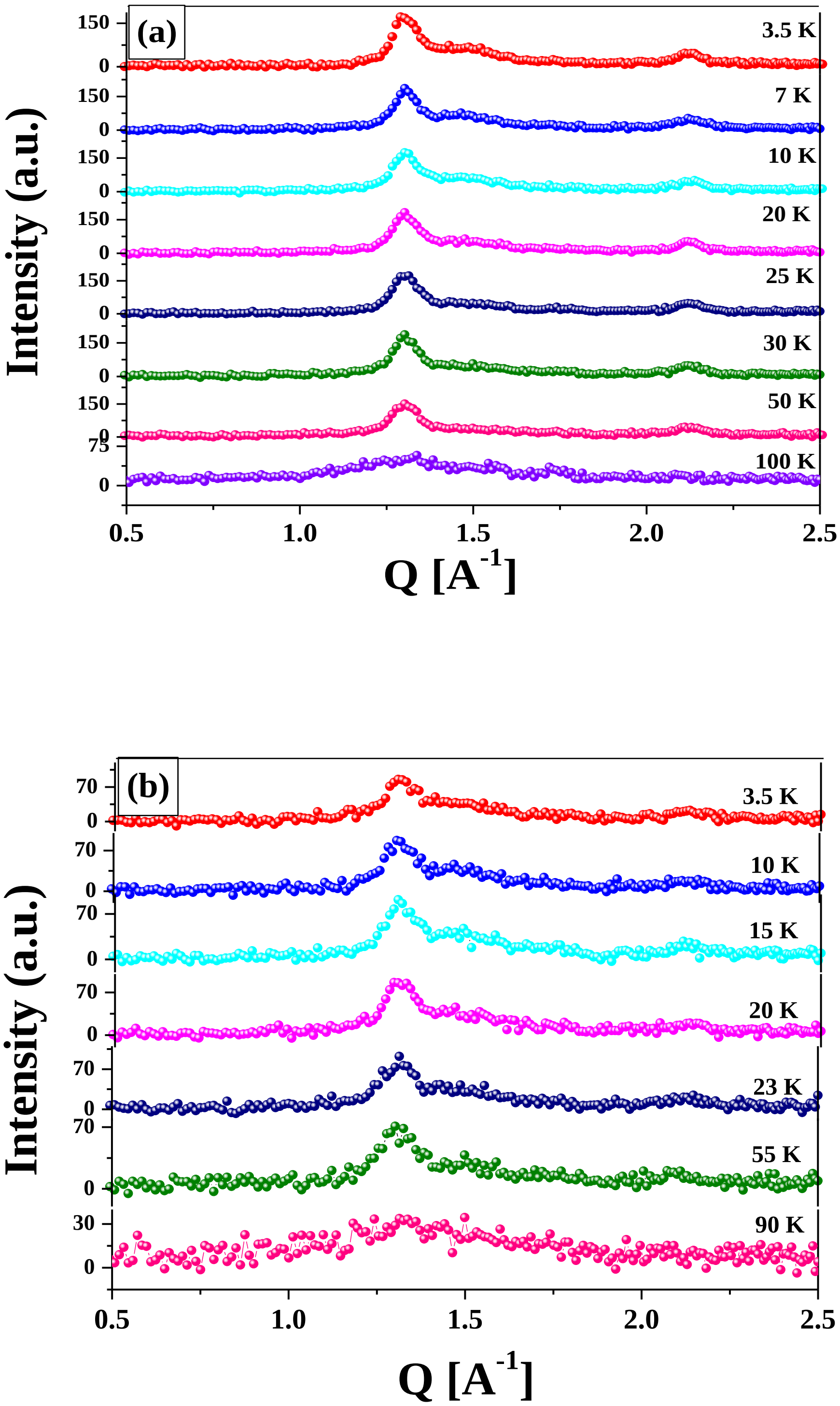

Fig. 6.2.2.3 Temperature dependence of magnetic scattering intensities of fundamental and satellite reflections for $Zn_xCo_{1-x}Cr_2O_4$ (a) x=0.05 and (b) x=0.1 respectively.

It indicates that the ferrimagnetic component exhibits long-range order below 100 K and 90 K for x=0.05 and 0.1 respectively. Due to broad and asymmetric nature of (111) peak, we have de-convoluted it into two peaks in order to calculate the intensity of fundamental reflection as well as satellite reflection.

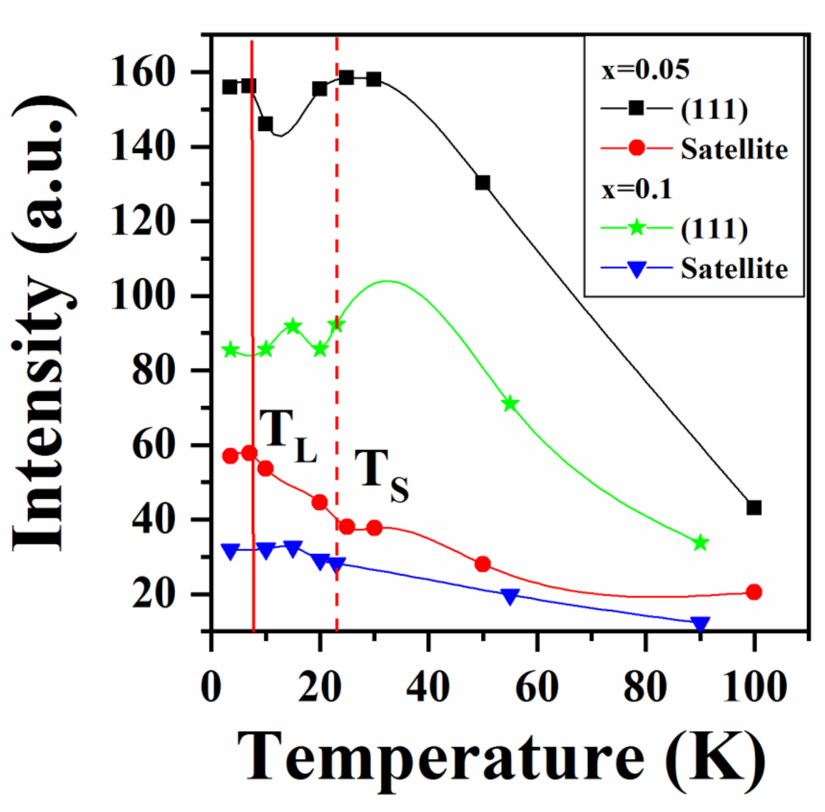

Fig. 6.2.2.4 Temperature dependence of integrated intensity of the fundamental magnetic (111) reflection and satellite reflection of x= 0.05 and x=0.1.

The intensity of the fundamental reflection (111) decreases with increase in Zn concentration in both x=0.05 and 0.1 as shown in Fig. 6.2.2.4. The intensity of (111) peak changes its slope at ~26 K and ~24 K for x=0.05 and 0.1 respectively which indicates spin-spiral transition, T_S. The variation in intensity at T_S is the evidence of the tilting of the magnetic moment. Though the intensity of the satellite peak is found to be weak in x=0.1, it is observed that the intensity increases slowly with decrease in temperature in both samples. The intensity is getting flat at 10 K with decrease in temperature which is noted as spin lock-in transition, T_L. Although no spin lock-in transition is reported from neutron scattering experiments done by Tomiyasu *et al* in our previous work on $CoCr_2O_4$, as well as in the present case we have demonstrated T_S and T_L from diffused neutron scattering [Tomiyasu et al. (2004)]. Atomic arrangement in both samples remains disordered even at very low temperature, resulting in a relatively flat diffusive background. As a consequence, we have observed non-saturation behavior of magnetization by applying external magnetic field of 140 kOe discussed later. A similar diffuse background due to magnetic disorder has been proposed by Golosovsky *et al.* [Golosovsky et al. (2001)].The correlation length of the spiral order (ξ) is calculated by taking the inverse of the half width at half-maxima (HWHM). The half width half-maxima of the satellite reflection is determined using Lorentzian distribution by the method of least square in x=0.05 and 0.1.

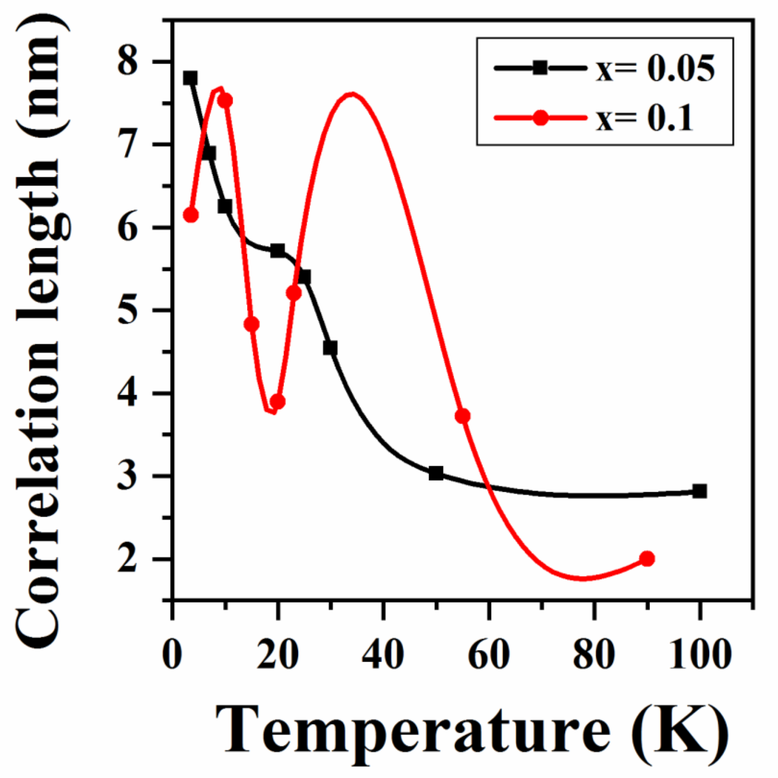

Fig. 6.2.2.5 Temperature dependence of correlation length of the spiral component for x= 0.05 and x=0.1 respectively. The values are obtained by taking the inverse of the half width half maxima.

The temperature dependent correlation length for x=0.05 and 0.1 is shown in Fig. 6.2.2.5. As temperature decreases, ξ increases slowly up to 30 K. Further, decrease in temperature down to 3.5 K lead to a sharp increase in correlation length. The value of ξ at 3.5 K is more than 6 nm for x=0.05 and 0.1 respectively, which are higher than 3.1 nm of single crystal $CoCr_2O_4$ [Tomiyasu et al. (2004)]. Yamasaki *et al.* investigate the low-temperature magnetic phase diagram of $CoCr_2O_4$ and have found that the compound undergoes a transition to a conical spin structure with an incommensurate propagation vector Q ~ (0.63, 0.63, 0) at T_N=26 K, and spin lock-in transition, T_L around 15 K [Yamasaki et al. (2006)]. Dwight *et al.* predicted that spiral ordering is incommensurate and the commensurate spiral order is observed due to some defects [Dwight et al. (1969)]. The spiral order observed in our case is twice than that of $CoCr_2O_4$ and is diffused in nature unlike in $CoCr_2O_4$ nanoparticles [Golosovsky et al. (2001)].We confirm that the long-range ferrimagnetic to paramagnetic transition as well as large spiral ordering after incorporation of Zn in $CoCr_2O_4$ in contrast to the short range spiral ordering observed in $CoCr_2O_4$ [Jagadish et al. (2016)].

6.2.2.3. Field dependent magnetization

The field dependent magnetization measurement is probed further in order to find out the relative alignments of the spins and their magnitude. The magnetization is measured after applying magnetic field of 140 kOe in x=0.05 and 0.1 at different temperatures such as 2, 20, 50 K, i.e. below T_C. The variation in Magnetization (M) with magnetic field (H) at 2 K, 20 K and 50 K is shown in Fig. 6.2.2.6 (a), (b) and (c) respectively. The magnetization doesn't saturate upto 140 kOe irrespective of measuring temperatures. The magnetization increases readily upto 20 kOe and then linearly increases upto 140 kOe. The non-saturation of magnetization results from the large contribution of disordered spins at the surface.

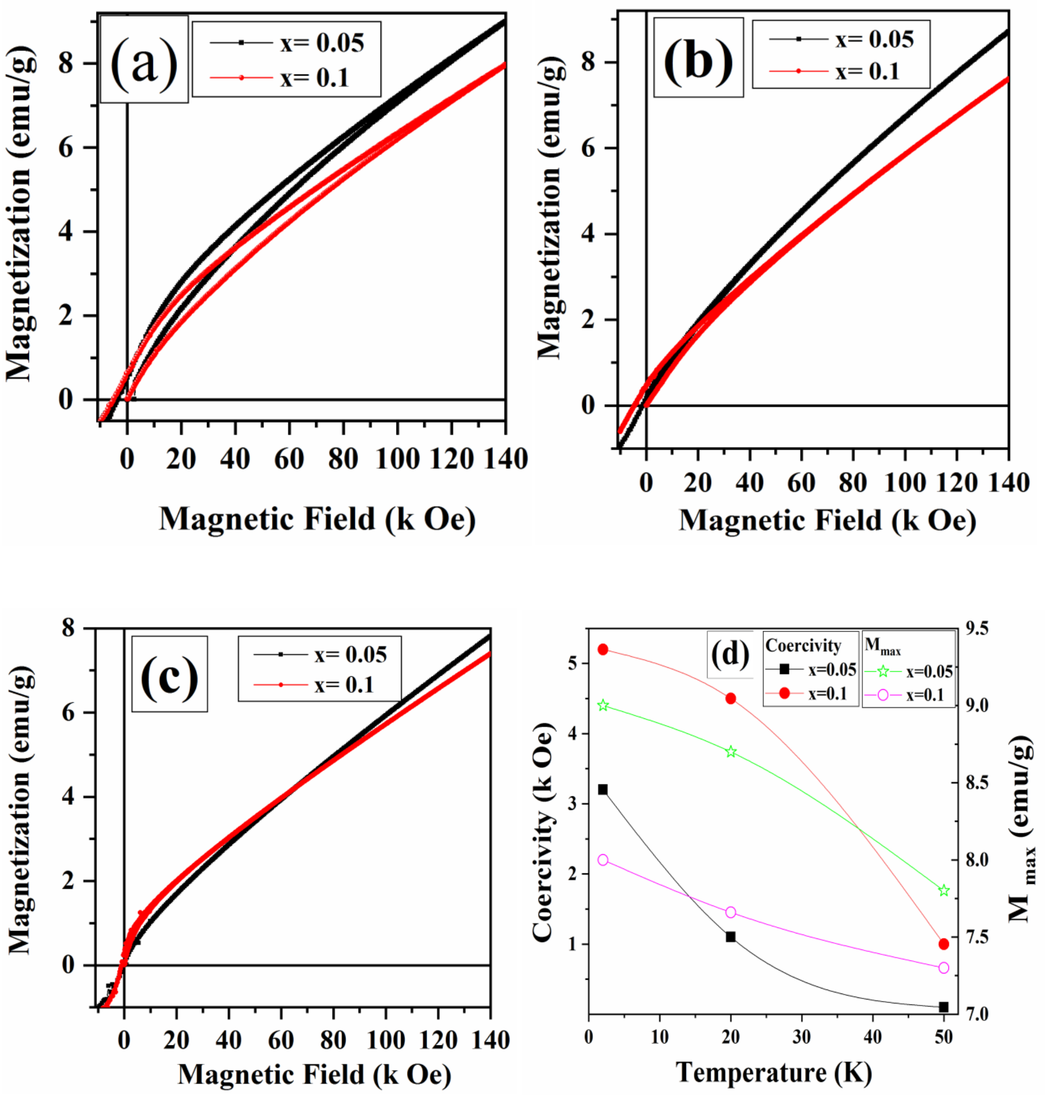

Fig. 6.2.2.6 Magnetic field (H) dependent magnetization at **(a)** 2 K, **(b)** 20 K and **(c)** 50 K for $Zn_xCo_{1-x}Cr_2O_4$ (x=0.05, 0.1). **Fig. 6.2.2.6 (d)** Show the temperature dependent coercivity and maximum magnetization for both samples. Coercivity and maximum magnetization are calculated from field dependent magnetization at 2 K.

Fig. 6.2.2.6 (d) depicts the temperature dependence of change in maximum magnetization at 140 kOe for both samples. One may note that, the magnetization measured at maximum applied field decreases with increase in temperature in both samples as expected. However, the difference in magnetization is uniformly maintained throughout the temperature range. Fig. 6.2.2.6 (d) depicts the temperature dependent coercivity for x= 0.05 and 0.1. With increase in Zn concentration from 0.05 to 0.1, the coercivity increases from 3.2 kOe to 5.2 kOe. The observed coercivity is found to be two orders magnitude higher than that of bulk $CoCr_2O_4$ at 2 K. Franco *et al.* have reported that Zn incorporation in $CoFe_2O_4$ spinel compounds results in decrease in saturation magnetization and coercivity [Franco et al. (2013)]. The decreasing trend is an indication of Co^{2+} is being replaced by Zn^{2+} ions in $Co_{1-x}Zn_xFe_2O_4$ mixed ferrite. However, although in the present case, we have incorporated Zn ions in similar spinel structure $CoCr_2O_4$, one may notice that, while the maximum magnetization decreases from 9 to 8 emu/g, the coercivity increases by 2 kOe at 2 K with an increase in non-magnetic Zn ion concentration from 0.05 to 0.1. This clearly indicates that B site ions play a significant role in producing such unusual behavior. We have further explained such behavior by considering different models like Neel's two sub-lattice model and Yafet- Kittel model used generally in ferrimagnetic materials.

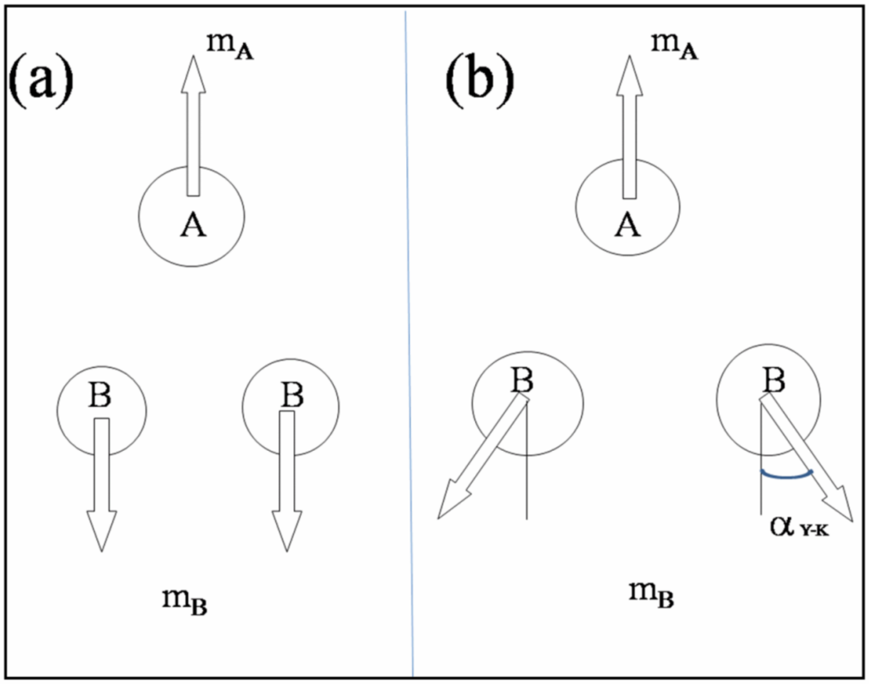

Fig. 6.2.2.7 Schematic representation of spin orientation at A and B sites for **(a)** collinear (Neel's Model) and **(b)** non-collinear (Y-K) Model.

According to the Neel's two sub-lattice model, the magnetic moments of ions on the A and B sub-lattices are aligned anti-parallel to each other and their spins have a collinear structure as shown in Fig. 6.2.2.7 (a). Increase in non-magnetic Zn^{2+} ions which occupy A-site while result in decrease in magnetic moment of A-site, the magnetic moment of B-site (Cr^{3+}) remains constant. The theoretical magnetic moment, $n_B^{th} = M_B - M_A$ has been calculated as 3.15 μ_B for x=0.05 and 3.3 μ_B for x=0.1. The experimental magnetic moment, n_B^{exp} is found to be one order magnitude less than the theoretical one. The reduction in magnetization could be due to the existence of random canting of spins at the surfaces due to nanometer size of the particles [Coey et al. (1971)]. The decrease in magnetic moment with increase in Zn concentration indicates a possibility of non-collinear spin structure which can be explained on the basis of three sub-lattice model suggested by Yafet-Kittel (Y-K) model [Yafet et al. (1952)]. According to Y-K model, the B lattice is divided into two sub-lattices i.e. B_1 and B_2. Each sub-lattice is having magnetic moments equal and each one is oppositely canted at the same angle, α_{YK} as shown in Fig. 6.2.2.7 (b). The net magnetic moment is given by $n_B^{exp} = M_B \cos \alpha_{YK} - M_A$. Where, n_B^{exp} is expressed in Bohr magneton. The Y-K angle (α_{YK}) is expressed as:

$$\alpha_{Y\text{-}K} = \mathrm{Cos}^{-1}\left(\frac{n_B^{exp} + M_A}{M_B}\right)$$

The non-zero Y-K angle (α_{YK}) suggests that, the magnetization behavior cannot be explained on the basis of Neel two sub-lattice model due to the presence of non-collinear spin structure at B site, which strengthens the B-B interaction at the cost of A-B interaction.[32] The collinear spin structure results to zero Y-K angles. We have estimated the Y-K angles using above equation and are found to be 57.5^o and 59.7^o for x=0.05 and 0.1 respectively. The non-zero Y-K angle thus confirms the non-collinear spin structure and favors triangular spin arrangement in B site. The increase in Y-K angle with increase in Zn concentration could be the origin of increase in coercivity with increasing Zn concentration. The increase in Y-K angle with increase in Zn concentration also supports the decrease in T_C observed from dc χ vs. T measurement.

In order to calculate the effective magnetic moment (μ_{eff}), the high temperature susceptibility data in paramagnetic region is used to fit the Curie-Weiss equation $\chi = \frac{C}{(T-\Theta_{CW})}$ Where C is the Curie constant and (Θ_{CW}) is the Curie-Weiss temperature. The effective magnetic moment is calculated using the relation $\mu_{eff} = (3CK_B/N)^{1/2}$, where C is the slope obtained from the inverse susceptibility versus temperature. The fitting parameters are shown in Table 6.2.2.

Table 6.2.2: Results from fitting the inverse magnetic susceptibility data to the Curie-Weiss equation to the high temperature inverse susceptibility data for $Zn_xCo_{1-x}Cr_2O_4$ (x = 0.05, 0.1). Θ_{cw} is taken as the x-intercept of the inverse susceptibility. *f* is defined as the absolute ration of Θ_{cw} to T_C.

x	**Quenched** (Spin-only) **μ_{eff} (μ_B)**	**Unquenched** (Spin+orbital) **μ_{eff} (μ_B)**	**Measured μ_{eff} = $(3CK_B/N)^{1/2}$ (μ_B)**	**Θcw (K)**	**Curie constant (C)**	**T_c (K)**	***f* = $\vert\Theta_{cw}\vert/T_c$**
0.05	6.7	7.46	6.68	-445	5.6	90	4.9
0.1	6.6	7.37	7.42	-360	6.9	87.4	4.1

The calculated values of μ_{eff} are 6.68 μ_B and 7.42 μ_B for x=0.05 and 0.1 respectively. As Zn content increases, magnetic moments decreases in sub-lattice A and increases in sub-lattice B. Hence, the μ_{eff} increases with Zn concentration. Further it is observed that, at 2 K, the maximum magnetic moment per atom (n_B^{exp}) in the direction of field is found to be an order of magnitude less than the magnetic moment obtained from the paramagnetic range (μ_{eff}). The large paramagnetic moment is also evidenced from the non-saturation behavior of magnetization at 140 kOe field which could be due to magnetic correlation in the paramagnetic regime [Kemei et al. (2012)].The orbital quenched (spin-only) moment is calculated using the relation ($\mu_S=2(S(S+1))^{1/2}$) for free ions Co^{2+} and Cr^{3+} (S=3/2) and is noted as 3.88 μ_B. For x=0.05, the total quenched moment is calculated using $((1-x)\mu_{Co}^2 + 2\,\mu_{Cr}^2\,)^{1/2}$. The obtained value of quenched moment (6.7 μ_B) is close to effective magnetic moment for x=0.05. In order to explain the higher μ_{eff} observed for x=0.1, the unquenched orbital contribution from Co^{2+} is considered and is calculated using the relation $\mu_{L+S} = [(4S(S+1)+L(L+1)]^{1/2}$. The unquenched moment obtained (7.37 μ_B) is close to μ_{eff} for x=0.1 (7.42 μ_B). In case of x=0.05, the measured μ_{eff} is close to quenched moment (6.7μ_B). While this may be unexpected for Co^{2+} in a tetrahedral coordination having no orbital degeneracy, the presence of low lying e^g, t^{2g} excited state could be a source for the increased moment [Lee et al. (2008)]. The frustration index, *f* is defined as the absolute ratio of $|\Theta_{cw}|/T_C$ and is calculated as 4.9 and 4.1 for x= 0.05 and 0.1 respectively.

6.2.2.4. Temperature dependent AC susceptibility

In order to examine the magnetically ordered state in these nanoparticles, ac susceptibility measurements (χ' and χ'') with varying temperature and frequency have been undertaken and results are shown in Fig. 6.2.2.7. The real (χ') and imaginary (χ'') parts of ac susceptibility at 3, 31, 231 and 966 Hz for x=0.05 and 0.1 are shown in Fig. 6.2.2.8 (a) and (b) respectively. The real part of ac susceptibility of x=0.05 exhibits a broad peak at T_B with a shift towards higher temperature with increase in frequency while it is found to be absent in x= 0.1.

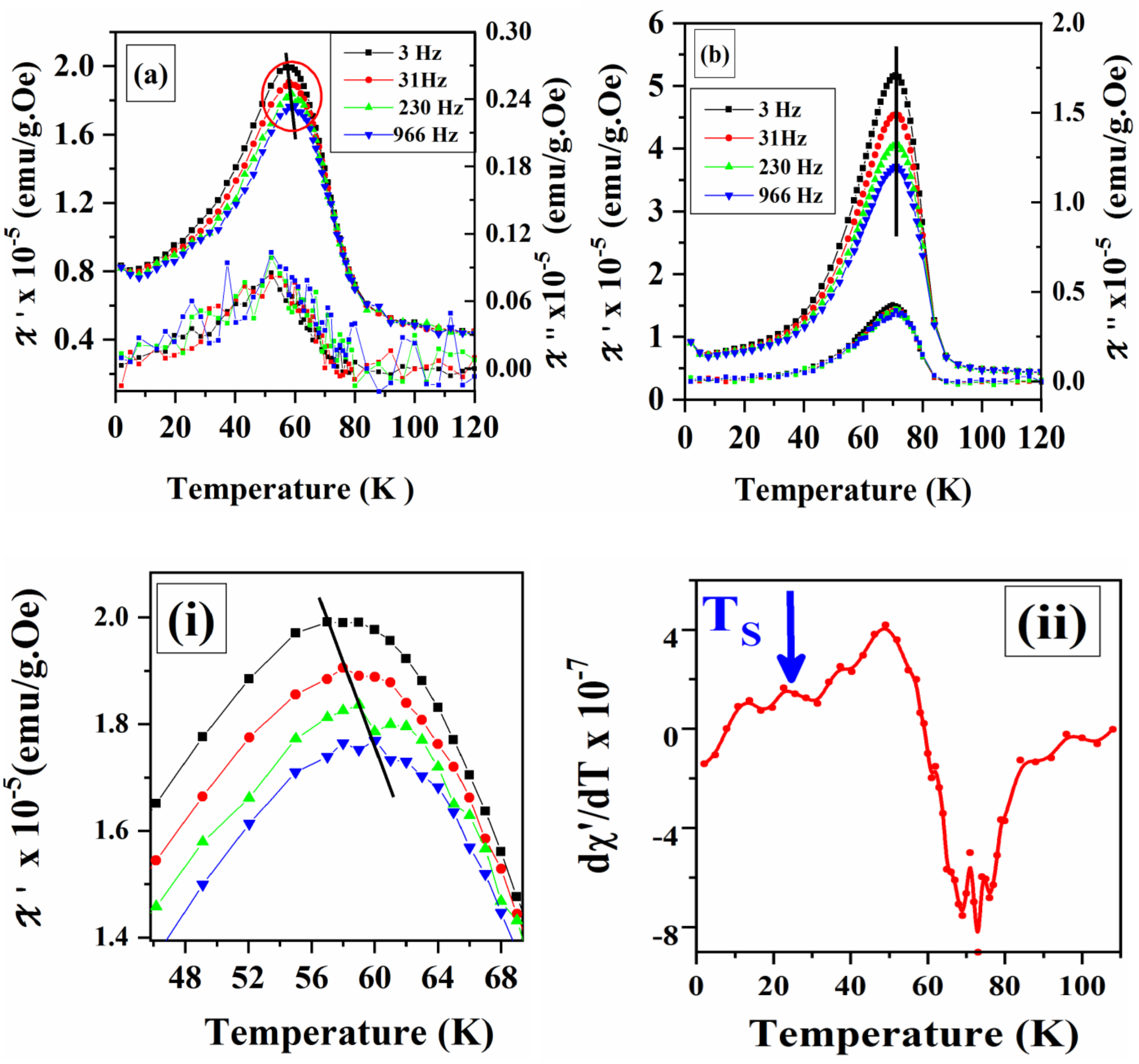

Fig. 6.2.2.8 Real and imaginary parts of ac susceptibility versus temperature at different frequencies 3, 31, 230 and 966 Hz for $Zn_xCo_{1-x}Cr_2\ O_4$ (a) x=0.05 and (b) x=0.1 respectively. Fig. 6.2.2.7 (i) depicts the expanded view of the peak shift with frequency for x=0.05. Fig. 6.2.2.8 (ii) depicts $\frac{d\chi'^{2}}{dT}$ versus temperature at 966 Hz for x=0.05.

Fig. 6.2.2.8 (ii) clearly denotes the spin-spiral transition (T_S) at 26 K for x=0.05 which is found to be absent in x=0.1. For x=0.05, the magnitude of χ' becomes smaller, and the low temperature tail of this peak decreases with increase in frequency. Such a frequency dependence of ac susceptibility is commonly observed in both spin glass and superparamagnetic systems. However, in our case, the shift in T_B with frequency is small

(~0.1) which eliminates the possibility of non-interacting superparamagnetic nature of the particles [Binder et al. (1986)].The frequency dependence of T_B explained using $\phi = \frac{\Delta T_B}{T_B \Delta log_{10}(f)}$ gives the value of ϕ as 0.02. In general, the value of ϕ lies in between 0.005-0.08, ~ 0.03 - 0.06 and 0.3 for spin glass (SG), cluster spin glass (CG) and non-interacting superparamagnetic (SPM) particles respectively [Mydosh et al. (1993); Calleja et al. (2007)]. The obtained value of 0.02 matches well with the SG rather than the non-interacting SPM particles. With increasing strength of interaction between the particles, one can encounter collective behavior. In order to understand the inter-cluster interaction and its effect on the fluctuation dynamics, we have further analyzed Neel-Arrhenius, Vogel-Fulcher and power law [Binder et al. (1986)]. According to Neel-Arrhenius law, the relaxation time for an assembly of non-interacting superparamagnetic (SPM) particles is expressed as $\tau = \tau_0 \exp(E_a/K_BT)$, Where E_a is the average anisotropy (activation) energy barrier equal to KV, K is the anisotropy constant and V is the volume of the particle. τ_0 is a time constant corresponds to the characteristic frequency.

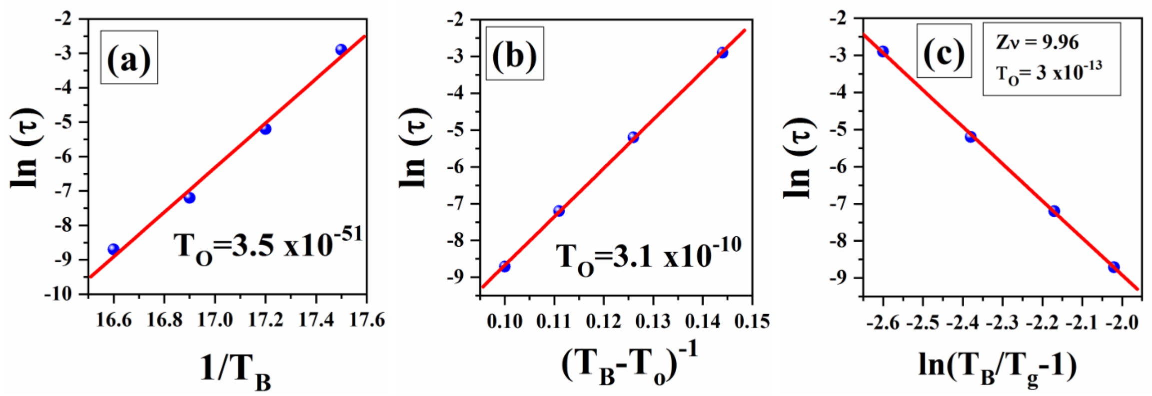

Fig. 6.2.2.9 (a) Relaxation time (τ) is fitted using Neel-Arrhenius law for $Zn_{0.05}Co_{0.95}Cr_2O_4$. **Fig.** 6.2.2.9 **(b)** and **(c)** depicts fitting using and Vogel-Fulcher's law and power law respectively.

The best fit is shown in Fig. 6.2.2.9 (a). The value of τ_0 is found to be 3.5x10^{-51}, an unphysical value which eliminates the possibility of the non-interacting superparamagnetic nature of the particles. Further Vogel-Fulcher's law, $\tau = \tau_0 \exp[\frac{-E_a}{K_B(T_B - T_o)}]$ has been analyzed to explain the frequency dependent shift of T_B. Where T_o is the Vogel-Fulcher temperature ($0<T_o<T_B$) which represents strength of the inter-particle interaction and is varied in steps of 0.2 K in order to fit the data. τ_0 of 3.1x10^{-10}s, obtained from the best fit (Fig. 6.2.2.9 (b)), is found to be three orders higher in magnitude than the spin-flip time of atomic magnetic moment (~10^{-13} s) which suggests CG behaviour. Further, the frequency dependent shift of the χ' fitted with power law: $\tau=\tau_0(T_f/T_g - 1)^{-z\nu}$ --------------(2)

Where $\tau_{o,}$ is the microscopic flipping time of the fluctuating spins, T_g is the spin-glass transition temperature, z is the dynamical exponent, and ν is the usual critical exponent for the correlation length. The best fit of equation (2), shown in Fig. 6.2.2.9 (c), gives the value of $z\nu$ as 9.9 which is of spin glass. The value of τ_0 obtained from the fit is 3x10^{-13}s is also consistent with the spin glass behavior. The interaction effect in nanoparticles studied by Poddar *et al*. shows that the strong dipolar interaction between nanoparticles would yield a spin-glass like behavior and the strength of interaction arises from the bulk crystalline and the surface anisotropy [Poddar et al. (2002)]. The randomly induced spin disorder in x=0.05 promotes the surface anisotropy and strengthens the dipolar interaction resulting to spin-glass nature. Hence for x=0.05, the coexistence of both CG and SG behavior of particles is confirmed from Vogel-Fulcher law and power law. In case of x=0.1, the magnetic moment of A sub-lattice decreases with Zn which weakens the surface spin disorder in nanoparticles and hence results in weak dipolar interaction. Thus we doesn't observe any dispersion of susceptibility with frequency in x=0.1.

6.4. Conclusions

In this chapter, we have studied the structure, cation distribution and magnetic properties of $Zn_xCo_{1-x}Cr_2O_4$ (x=0.05, 0.1) nanoparticles of size 10 nm which were synthesized through conventional co-precipitation technique. XRD patterns confirmed the cubic spinel structure without any impurity phase. Lattice parameter decreased with increase in Zn concentration, due to less ionic nature of Zn than Co, and/or due to decrease in A-B repulsion. Cation distribution of $Zn_xCo_{1-x}Cr_2O_4$ studied through EXAFS confirmed that while Cr^{3+} ions preferred B site, Zn^{2+} and Co^{2+} ions occupied the A site. From dc magnetization and diffused neutron scattering, with increase in x from 0.05 to 0.1, we revealed that the paramagnetic to ferrimagnetic transition, T_C, decreased from 90 K to 87.4 K, T_S from 26 K to 24 K and the spin lock-in transition, T_L observed at 10 K remained unchanged. Temperature dependent ac magnetic susceptibility measurement showed the dispersion behavior with frequency for x=0.05 which was found to be absent in x=0.1. The phenomenological models like Vogel-Fulcher, power law were fitted and coexistence of spin-glass and cluster glass in x=0.05 was confirmed. Neel's two sub-lattice model failed to explain the decrease in saturation magnetization with increase in Zn concentration measured from hysteresis loop at 2 K. This was well explained by considering the three sub-lattice model suggested by Yafet-Kittel (Y-K). The increase in Y-K angles with increase in Zn concentration further indicated the triangular spin arrangement in B site resulting in decreasing A-B exchange interaction hence decrease in T_C.